ELSEVIER

Comput. Methods Appl. Mech. Engrg. 130 (1996) 33–45

Computer methods in applied mechanics and engineering

A 2D Chebyshev differential operator for the elastic wave equation

José M. Carcione

Osservatorio Geofisico Sperimentale, P.O. Box 2011, Opicina, I-34016 Trieste, Italy

Received 13 December 1993; revised 22 May 1995

Abstract

This work analyses the performance of a two-dimensional Chebyshev differential operator for solving the elastic wave equation. The technique allows the implementation of non-periodic boundary conditions at the four boundaries of the numerical mesh, which requires a special treatment of these conditions based on one-dimensional characteristics. In addition, spatial grid adaptation by appropriate one-dimensional coordinate mappings allows a more accurate modeling of complex media, and reduction of the computational cost by controlling the minimum grid spacing. The examples illustrate the ability of the method to simulate Rayleigh waves around a corner and adapt the mesh to the model geometry. In addition, a domain decomposition example shows how the boundary treatment handles wave propagation from one mesh to another mesh.

1. Introduction

The use of spectral differential operators for solving the wave equation is an important tool in geophysical problems. Several works are based on the Fourier–Chebyshev operator. In particular, the articles by Kosloff et al. [1] and Tessmer et al. [2] treated the elastic wave equation in Cartesian coordinates, and Kessler and Kosioff [3] solved the acoustic wave equation in cylindrical coordinates by using the Chebyshev method in the radial direction and the Fourier method in the azimuthal direction. Carcione [4] simulated anelastic Rayleigh waves by means of the same operator. These works, which use the Fourier method in one of the directions, are restricted to periodic boundary conditions in that direction.

In a relatively recent article, Raggio [5] introduced a 2D pseudospectral Chebyshev scheme to model wave propagation in inhomogeneous acoustic media. This scheme suffers from two major disadvantages. In the first place, the grid points are restricted to the Gauss–Lobatto collocation points, and secondly, as Raggio points out, the clustering of the Chebyshev points near the interval end points greatly restricts the time step of the time integration scheme.

In this work, we extend the modeling scheme from the acoustic to the elastic rheology. We use a mapping transformation for each Cartesian coordinate which circumvents the severe stability condition of the integration method and distributes grid points in arbitrary locations. The 2D physical domain is discretized at a set of points obtained from a 2D Chebyshev grid (computational domain) after application of two 1D mapping transformations to each Cartesian coordinate. As mentioned above, the need of these transformations comes from the fact that the Gauss–Lobatto collocation points are very densely distributed at the end points of the mesh, and therefore impose a very restrictive stability condition on the time integration scheme, with time steps of the order $O(N^{-2})$ where N is the number of grid points along each Cartesian direction. By stretching the mesh we increase the grid spacing and

SSDI 0045-7825(95)00896-9

use time steps of the order $O(N^{-1})$ [6]. Furthermore, these transformations can be used for spatial grid adaptation [7, 8] in the sense that the collocation points can be redistributed and properly concentrated in regions with steep velocity gradients, fine layering, complex interface geometries and physical boundary conditions like the surface of the Earth. For instance, an interface defined in a coarse grid may introduce considerable errors into the computed reflection and transmission coefficients due to the presence of Gibbs oscillations between collocation points [7]. Raggio [5] found that this error is proportional to the square of the grid spacing.

Unlike the Fourier method, the Chebyshev pseudospectral method facilitates the implementation of general boundary conditions at the four boundaries of the mesh. For instance, in Lamb's problem [9], the upper boundary satisfies traction-free boundary conditions, and the other boundaries satisfy open radiation conditions. However, solutions computed by a direct implementation of the boundary conditions are strongly unstable. This problem is solved by modifying the wave equation by imposing the correct behavior on the 1D characteristics normal to the boundaries. This method implies that a different wave equation is solved at these boundaries [10, 11]. For example, the open or non-reflecting boundary condition is imposed by eliminating the incoming characteristics. In addition, absorbing strips are used to avoid residual non-physical reflections coming from directions out of the normal.

One of the advantages of this non-periodic mesh is the possibility of partitioning a large physical domain into several subdomains where the grid spacing, stretching parameters, number of grid points and rheology of the medium can be controlled independently. The subdomains can be joined by imposing the appropriate continuity conditions at the boundaries. This is the basis of domain decomposition techniques [12] where each subregion can be solved in a different CPU of a parallel computer, thus reducing the computational time.

2. The wave equation

The wave equation is based on the equations of momentum conservation combined with the constitutive relations for 2D isotropic and elastic media [13]. The velocity-stress formulation in the (x, y) plane takes the following matrix form

$$\frac{\partial \boldsymbol{v}}{\partial t} = \boldsymbol{A}\frac{\partial \boldsymbol{v}}{\partial x} + \boldsymbol{B}\frac{\partial \boldsymbol{v}}{\partial y} + \boldsymbol{s}, \tag{1}$$

where

$$\boldsymbol{v} = [v_x, v_y, \sigma_{xx}, \sigma_{yy}, \sigma_{xy}]^{\mathrm{T}}, \tag{2}$$

is the unknown vector,

$$\boldsymbol{A} = \begin{bmatrix} 0 & 0 & \rho^{-1} & 0 & 0 \\ 0 & 0 & 0 & 0 & \rho^{-1} \\ E & 0 & 0 & 0 & 0 \\ \lambda & 0 & 0 & 0 & 0 \\ 0 & \mu & 0 & 0 & 0 \end{bmatrix}, \tag{3}$$

$$\boldsymbol{B} = \begin{bmatrix} 0 & 0 & 0 & 0 & \rho^{-1} \\ 0 & 0 & 0 & \rho^{-1} & 0 \\ 0 & \lambda & 0 & 0 & 0 \\ 0 & E & 0 & 0 & 0 \\ \mu & 0 & 0 & 0 & 0 \end{bmatrix}, \tag{4}$$

and

$$\boldsymbol{s} = [f_x, f_y, 0, 0, 0]^{\mathrm{T}}, \tag{5}$$

is the body force vector. The unknown fields are the particle velocities v_x and v_y, and the stress components σ_{xx}, σ_{yy} and σ_{xy}. The elastic properties of the medium are defined by the Lame constants λ and μ, $E = \lambda + 2\mu$ and ρ is the density.

3. The 2D Chebyshev differential operator

The differential operator is based on the Chebyshev method whose collocation points define the numerical mesh of the computational domain (Section 3.1). From this, the physical domain is obtained after mapping transformations which circumvent the severe stability condition of the time integration scheme and yield spatially adaptive grids (Section 3.2). The implementation of boundary conditions requires a special treatment based on characteristics variables (Section 3.3).

3.1. Chebyshev collocation method

The computational domain is a square region $(\xi, \eta) \in [1, -1] \times [1, -1]$, where the grid distribution is defined by the Chebyshev Gauss–Lobatto points. Let us assume that the pair (ζ, N) represents either (ξ, N_x) or (η, N_y), where N_x and N_y are the number of grid points in the x- and y-directions, respectively. A field variable $u(\zeta)$, $-1 \leqslant \zeta \leqslant 1$, can be expanded into Chebyshev polynomials $T_n(\zeta)$ as

$$u(\zeta_j) = \sum_{n=0}^{N}{}'' a_n T_n(\zeta_j), \tag{6}$$

where $\zeta_j = \cos(\pi j/N)$, $j = 0, 1, \ldots, N$, are the Gauss–Lobatto collocation points, and $\sum''$ halves the first and last terms. The first-order derivative of u is given by

$$\frac{\partial u}{\partial \xi} = \sum_{n=0}^{N}{}'' b_n T_n(\zeta_j), \qquad b_{n-1} = b_{n+1} + 2n a_n, \quad n = N, N-1, \ldots, 1, \tag{7}$$

initiating the recursion equation with $b_{N+1} = b_N = 0$ [14]. The spatial derivative is computed via a variant of the fast Fourier transform (FFT) for the cosine transform. A detailed analysis of the different methods to compute the cosine transform can be found in Raggio [5].

3.2. Coordinate mappings

The uneven distribution of points of the Chebyshev differential operator has two main disadvantages. In the first place, the stability condition and the accuracy of the time integration scheme depend on the minimum grid spacing of the mesh. The dense concentration of points of the Chebyshev mesh at the boundaries requires time steps of the order $O(N^{-2})$, making the modeling algorithm highly inefficient. Although, as Solomonoff and Turkel [15] pointed out, for global differential operators, there is no direct correlation between the minimum grid spacing and the maximum allowable time step, increasing the minimum spacing effectively reduces the computational cost [6]. In second place, there is no justification for concentrating points in regions where there are not small inhomogeneities to model. In this sense, grid adaptation is fully justified.

These problems are solved by expanding the solution as a finite sum of non-polynomial basis functions. This is achieved by 1D transformations or stretching functions which, when applied to the Gauss–Lobatto points, yield a numerical grid that can be adapted to the particular structure of the model and boundary conditions. Lamb's problem, for instance, requires a mapping with free surface boundary conditions at $y = 0$, and open (non-reflecting) radiation conditions at the other boundaries. Along the y-direction, a non-symmetric stretching function is used, with grid dense enough at the surface to sample the wavefield appropriately to model the boundary condition, but coarse enough to avoid the severe stability condition. At the bottom, this condition is not necessary, and a coarser grid extends as far as possible the physical domain. Moreover, the transformations allow time steps of order $O(N^{-1})$, thus considerably reducing the computer time.

We consider the following coordinate transformation from the computational to the physical domain:

$$z_j = z_{\max}\left[\frac{q(\zeta_j) - q(1)}{q(-1) - q(1)}\right], \qquad j = 0, 1, \ldots, N \tag{8}$$

mapping the interval $[1, -1]$ onto the interval $[0, z_{\max}]$, where z represents x or y, such that the physical

domain is $(x, y) \in [0, x_{\max}] \times [0, y_{\max}]$. The function

$$q = q(\zeta, \boldsymbol{\alpha}) \tag{9}$$

is a family of transformations, where $\boldsymbol{\alpha}$ is a vector of parameters defining the mapping.

The spatial derivative of a field variable in the physical domain is then given by

$$\frac{\partial u}{\partial z} = \frac{\partial u}{\partial \zeta}\frac{\mathrm{d}\zeta}{\mathrm{d}z} = \left[\frac{q(-1) - q(1)}{z_{\max}}\right]\frac{\mathrm{d}\zeta}{\mathrm{d}q}\frac{\partial u}{\partial \zeta}. \tag{10}$$

Examples of mapping functions q are the following:

(1) The non-symmetric function [6]

$$q(\zeta) = -|r|^{-1/2}\arcsin\left(\frac{2\zeta r + s}{\sqrt{s^2 - 4r}}\right), \tag{11}$$

where $r = 0.5\alpha^{-2}(\beta^{-2} + 1) - 1$ and $s = 0.5\alpha^{-2}(\beta^{-2} - 1) - 1$ with $\boldsymbol{\alpha} = (\alpha, \beta)$. Since

$$\frac{\mathrm{d}\zeta}{\mathrm{d}q} = \sqrt{1 + s\zeta + r\zeta^2}, \tag{12}$$

it can be seen that the amount of grid stretching at $\zeta = -1$ is $\mathrm{d}q/\mathrm{d}\zeta = \alpha$, and that the stretching at $\zeta = 1$ is $\mathrm{d}q/\mathrm{d}\zeta = \alpha\beta$.

(2) A symmetric mapping function is given by

$$q(\zeta) = \frac{\arcsin(\gamma\zeta)}{\arcsin(\gamma)}, \tag{13}$$

satisfying $q(1) = 1$ and $q(-1) = -1$. Here, $\boldsymbol{\alpha} = \gamma$, and

$$\frac{\mathrm{d}\zeta}{\mathrm{d}q} = \frac{\arcsin(\gamma)}{\gamma}\sqrt{1 - \gamma^2\zeta^2}. \tag{14}$$

This mapping, like the previous one, stretches the mesh at the boundaries. When $\gamma \to 0$, we obtain the Gauss–Lobatto collocation points, and $\gamma \to 1$ gives equally distributed points as in the Fourier differential operator. The mapping improves the π criterion for resolving the maximum wavenumber to almost two points per minimum wavelength, as in the Fourier case. A detailed analysis of resolution and accuracy of the 1D differential operator constructed with this transformation is given by Kosloff and Tal-Ezer [6].

(3) A non-symmetric transformation introduced by Augenbaum [7] is

$$q(\zeta) = \frac{\pi\delta - 2p}{2p\delta - \pi}, \qquad p = \arctan\left[\epsilon\tan\left(\frac{\pi\zeta}{2}\right)\right], \tag{15}$$

with $\boldsymbol{\alpha} = (\delta, \epsilon)$ and

$$\frac{\mathrm{d}\zeta}{\mathrm{d}q} = \frac{(2p\delta - \pi)^2}{\pi^2\epsilon(1 - \delta^2)}\left[\cos^2\left(\frac{\pi\zeta}{2}\right) + \epsilon^2\sin^2\left(\frac{\pi\zeta}{2}\right)\right], \tag{16}$$

where $\epsilon > 0$ and $|\delta| < 1$. The parameter ϵ controls the magnitude of the coordinate stretching (or compression) about a point determined by δ. For $\zeta = \pm 1$ the amount of stretching is given by

$$\frac{\mathrm{d}\zeta}{\mathrm{d}q} = \frac{1 \mp \delta}{1 \pm \delta}\epsilon. \tag{17}$$

Other non-symmetric mapping functions can be found in [6, 16]. Note that these coordinate transformations imply that we are no longer using polynomial approximation for the solution in the physical space.

3.3. Boundary conditions

Each time the right-hand side of Eq. (1) is computed, the boundary conditions are implemented. However, a direct application of these conditions gives unstable solutions. The global character of the

spectral differential operator implies that an incorrect implementation of the boundary conditions immediately affects the entire domain [17]. This problem is solved by decomposing the wavefield into one-way modes (or characteristics) perpendicular to the boundaries, and modifying these modes according to the boundary conditions. The method was recently applied by Thompson [18] to fluid dynamic problems and by Carcione [10, 11] to the wave equation. The implementation of the boundary conditions along a given direction requires the characteristic equation corresponding to Eq. (1) in that direction. Let us consider the boundary normal to the y-direction. Eq. (1) can be expressed as

$$\frac{\partial \boldsymbol{v}}{\partial t} = \boldsymbol{B}\frac{\partial \boldsymbol{v}}{\partial y} + \boldsymbol{s}_y, \qquad \boldsymbol{s}_y = \boldsymbol{A}\frac{\partial \boldsymbol{v}}{\partial x} + \boldsymbol{s}. \tag{18}$$

After diagonalization of matrix $\boldsymbol{B}$ as $\boldsymbol{B} = \boldsymbol{S}\boldsymbol{\Lambda}\boldsymbol{S}^{-1}$, Eq. (18) can be written as

$$\frac{\partial \boldsymbol{v}}{\partial t} = \boldsymbol{S}\mathcal{H} + \boldsymbol{s}_y, \tag{19}$$

the characteristic equation, where

$$\mathcal{H} = \boldsymbol{\Lambda}\boldsymbol{S}^{-1}\frac{\partial \boldsymbol{v}}{\partial y} \tag{20}$$

are the characteristic variables. $\boldsymbol{\Lambda}$ is a diagonal matrix formed with the eigenvalues of $\boldsymbol{B}$, λ_i, $i = 1, \ldots, 8$, related to the phase velocities of the outgoing and incoming wave modes, such that $\mathcal{H}$ represents each decoupled characteristic mode in the y-direction. Eq. (19) completely defines $\partial \boldsymbol{v}/\partial t$ at the boundaries in terms of the decoupled outgoing and incoming modes. The characteristics $\mathcal{H}_i$ with $\lambda_i > 0$, represent traveling modes in the positive direction of the coordinate axes, and vice versa for those characteristics with $\lambda_i < 0$. Having this in mind, the incoming modes are those quantities which point into the computational domain. These characteristics are computed from the boundary conditions while the outgoing modes are not modified, and replaced back into Eq. (19) to get the equations for the boundaries. The directions of the characteristics at the boundaries are illustrated in Fig. 1 (those quantities between parentheses are computed from the boundary conditions). In the following, the boundary equations for the upper (upper sign) and lower (lower sign) boundaries of the numerical mesh are given.

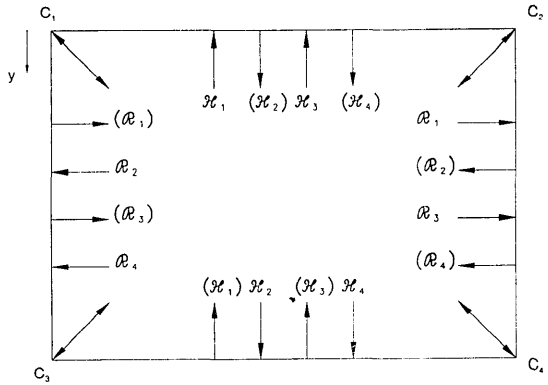

Fig. 1. Horizontal ($\mathcal{R}$) and vertical ($\mathcal{H}$) characteristics at the boundaries of the numerical mesh. The characteristics at the corners are also indicated. The first and second ones corresponds to the compressional waves while the third and fourth to the shear waves. These quantities between parentheses (the incoming modes) are computed from the boundary conditions.

The Neumann boundary equations are

$$\dot{v}_x^{\text{new}} = \dot{v}_x^{\text{old}} + \frac{1}{Z_S}(\pm\dot{\sigma}_{xy}^{\text{old}} - \dot{f}), \tag{21}$$

$$\dot{v}_y^{\text{new}} = \dot{v}_y^{\text{old}} \pm \frac{1}{Z_P}(\dot{\sigma}_{yy}^{\text{old}} - \dot{g}), \tag{22}$$

$$\dot{\sigma}_{xx}^{\text{new}} = \dot{\sigma}_{xx}^{\text{old}} - \frac{\lambda}{E}(\dot{\sigma}_{yy}^{\text{old}} - \dot{g}), \tag{23}$$

$$\dot{\sigma}_{yy}^{\text{new}} = \dot{g}, \tag{24}$$

$$\dot{\sigma}_{xy}^{\text{new}} = \pm\dot{f}, \tag{25}$$

where f and g are time-dependent functions, and $Z_P = \sqrt{(\lambda + 2\mu)\rho}$ and $Z_S = \sqrt{\mu\rho}$ are the compressional and shear impedances. A dot above a variable denotes time differentiation. The superscript 'old' indicates the variables given by Eq. (1), and the superscript 'new' refers to the variables of the left-hand side of Eq. (18) after modification of the incoming characteristics. In practice, at every time step and after application of the differential operator, the vector of field variables is modified according to the boundary equations. When $f = g = 0$, we have the free-surface boundary conditions. The method can be used also to excitate a source function at a given point of the boundary. For instance, $f = 0$, and $\dot{\sigma}_{yy}(\boldsymbol{x}_0, t) = \dot{s}(t)$ is a vertical force located at $\boldsymbol{x}_0$ with time history $g(t)$.

The Dirichlet boundary equations are

$$\dot{v}_x^{\text{new}} = \dot{v}, \tag{26}$$

$$\dot{v}_y^{\text{new}} = \pm\dot{w}, \tag{27}$$

$$\dot{\sigma}_{xx}^{\text{new}} = \dot{\sigma}_{xx}^{\text{old}} + \frac{\lambda}{E}(\dot{\sigma}_{yy}^{\text{old}} - \dot{\sigma}_{yy}^{\text{old}}), \tag{28}$$

$$\dot{\sigma}_{yy}^{\text{new}} = \dot{\sigma}_{yy}^{\text{old}} + Z_P(\pm\dot{v}_y^{\text{old}} - \dot{w}), \tag{29}$$

$$\dot{\sigma}_{xy}^{\text{new}} = \dot{\sigma}_{xy}^{\text{old}} \pm Z_S(\dot{v}_x^{\text{old}} - \dot{v}), \tag{30}$$

where v and w are time dependent functions. For instance, rigid boundary conditions imply $w = v = 0$.

The non-reflecting boundary equations are

$$\dot{v}_x^{\text{new}} = \frac{1}{2}\left(\dot{v}_x^{\text{old}} \pm \frac{1}{Z_S}\dot{\sigma}_{xy}^{\text{old}}\right), \tag{31}$$

$$\dot{v}_y^{\text{new}} = \frac{1}{2}\left(\dot{v}_y^{\text{old}} \pm \frac{1}{Z_P}\dot{\sigma}_{yy}^{\text{old}}\right), \tag{32}$$

$$\dot{\sigma}_{xx}^{\text{new}} = \dot{\sigma}_{xx}^{\text{old}} - \frac{\lambda}{2E}(\dot{\sigma}_{yy}^{\text{old}} \mp Z_P\dot{v}_y^{\text{old}}), \tag{33}$$

$$\dot{\sigma}_{yy}^{\text{new}} = \frac{1}{2}(\dot{\sigma}_{yy}^{\text{old}} \pm Z_P\dot{v}_y^{\text{old}}), \tag{34}$$

$$\dot{\sigma}_{xy}^{\text{new}} = \frac{1}{2}(\dot{\sigma}_{xy}^{\text{old}} \pm Z_S\dot{v}_x^{\text{old}}), \tag{35}$$

The equations for the left boundary can be obtained from the lower boundary equations by substituting $x \to y$ and $y \to x$. Similarly, the equations for the right boundary are obtained from the left boundary equations by substituting $x \to -x$, where in this case, $v_x \to -v_x$ and $\sigma_{xy} \to -\sigma_{xy}$.

For the corner points, we use an ad hoc treatment introduced by Lie [19] who defined the 'normal to the corner point' inwards and bisecting the angle between the adjacent boundary lines. For a rectangular mesh this angle is a multiple of $\pi/4$ depending on the corner point. For example, let the y'-direction (system S') make an angle $\pi/4$ with the y-axis (system S) where the problem is solved. The boundary treatment is applied to the variables in system S' since the method uses the characteristics normal to the boundaries. We proceed as follows: after calculation of the right-hand side of Eq. (1), giving, say, $\boldsymbol{v}_0$, we compute $\boldsymbol{v}_0'$ by rotating the particle velocities and stresses from S to S' by using [20]

$$\begin{bmatrix} v_x' \\ v_y' \end{bmatrix} = \frac{1}{\sqrt{2}} \begin{bmatrix} 1 & 1 \\ -1 & 1 \end{bmatrix} \begin{bmatrix} v_x \\ v_y \end{bmatrix}, \tag{36}$$

and

$$\begin{bmatrix} \sigma_{xx}' \\ \sigma_{yy}' \\ \sigma_{xy}' \end{bmatrix} = \frac{1}{2} \begin{bmatrix} 1 & 1 & 2 \\ 1 & 1 & -2 \\ -1 & 1 & 0 \end{bmatrix} \begin{bmatrix} \sigma_{xx} \\ \sigma_{yy} \\ \sigma_{xy} \end{bmatrix}. \tag{37}$$

Then, we apply the boundary treatment to vector $\boldsymbol{v}_0'$ and calculate the new $\boldsymbol{v}_0$ by the inverse rotation transformations.

4. Examples

The first example simulates Lamb's problem in order to check the accuracy of the Chebyshev operator. When the source is very close to the free surface, the high amplitude of the Rayleigh wave represents a challenge for the boundary treatment. The second example illustrates wave propagation through a surface step in order to test the characteristic approach applied to the corner points. A third example computes seismograms produced by a stack of fine layers modeled by refining the grid points at the center of the numerical mesh. Finally, the last example illustrates wave propagation in a multi-domain mesh.

4.1. Lamb's problem

We consider a Poisson solid with compressional and shear velocities $c_P = \sqrt{E/\rho} = 2000$ m/s, $c_S = \sqrt{\mu/\rho} = 1155$ m/s, respectively, with a density of $\rho = 2$ g/cm^3. We solve the problem in the ultrasonic range, but since it is elastic, the results can be scaled to any frequency range. The source is a vertical impact having a Ricker wavelet time-history with central frequency $f_0 = 110$ kHz.

The calculations use a numerical mesh with $N_x = 121, N_y = 81$, with the mapping function equation (13) for the x coordinate and the mapping function equation (11) for the y coordinate. The dimensions of the physical space after the transformations are $x_{\max} = 233.5$ mm and $y_{\max} = 146$ mm, with maximum grid sizes of $\mathrm{d}x_{\max} = \mathrm{d}y_{\max} = 2$ mm at the center of the mesh. The stretching parameters are $\gamma = 0.999$ for the x-direction, and $\alpha = 4.86$, $\beta = 2$ for the y-direction. The mesh has free surface boundary conditions applied to the upper boundary and open radiation conditions to the other boundaries. Since for non-vertical incidence the incoming waves are not completely eliminated, absorbing strips of length 18 grid points are used at the sides and lower boundary to eliminate the residual non-physical reflections [21]. The vertical force is applied at grid point 24 ($x = 37$ mm) at a depth of $y = 0.186$ mm (second grid point), which is very close to the surface. This depth is small compared to the dominant wavelength of the signal which for shear waves is approximately 10 mm. The solution is propagated to 0.2 ms with a time step of 0.1 μs, by using a 4th-order Runge–Kutta integration scheme [4]. This time step is of the order of the time step which would be used with the Fourier method.

Comparisons between numerical and analytical solutions are shown in Fig. 2, where the coordinates of the receivers relative to the source are in (a) and (b), (72,0) mm, and in (c) and (d), (72,29) mm. As can be seen from the pictures, the matching between solutions is excellent. The non-causal event before 0.02 ms occurs near the surface when the source reaches its maximum amplitude. The polarity of the noise changes in the x-direction at every grid point. This resembles the behavior of the Nyquist

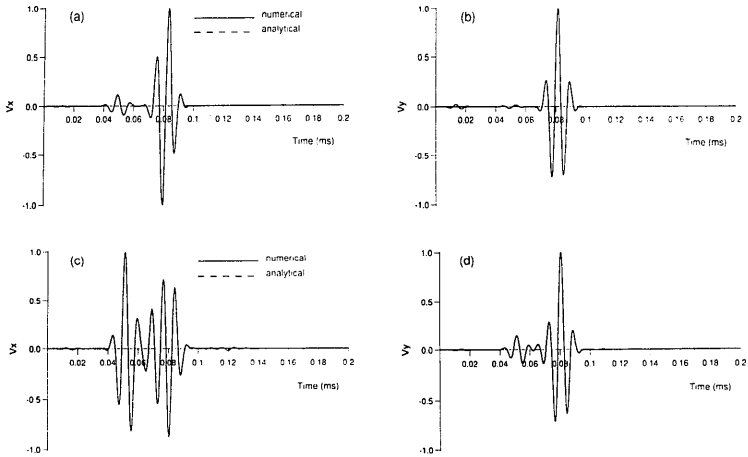

Fig. 2. Comparison between numerical and analytical solutions for Lamb's problem, where the coordinates of the receivers with respect to the source are in (a) and (b), (72,0) mm, and in (c) and (c), (72,29) mm. The matching is virtually perfect.

component. For display purposes, the noise can be eliminated by summing the solutions of contiguous grid points. This effect is probably caused by the so-called Runge phenomenon [22] which reflects in strong oscillations of the Chebyshev coefficients near the interval end points [5]. This problem takes place in equally spaced grids, so the cause could be too much stretching of the grid points at the surface. An elaborate analysis of this phenomenon will be given in a future paper.

4.2. *Step problem*

We consider the same physical properties, source type and number of grid points as the previous example. The model is a surface step whose physical mesh is illustrated in Fig. 3, where the upper and right boundaries satisfy traction-free conditions. The mappings functions are given by Eq. (11) for both

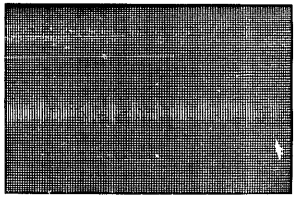

Fig. 3. Numerical mesh of the physical space for the step problem. The upper and right boundaries, which form the step, satisfy free surface conditions. The mesh is constructed with two one-dimensional mapping transformation based on Eq. (11).

cartesian coordinates with $\alpha = 4.86$ and $\beta = 2$, where $x_{max} = 225.5$ mm. As can be appreciated in Fig. 3, the mesh is denser at the step in order to correctly model the free surface condition. The lower and left boundaries satisfy open radiation conditions. The vertical force is applied at grid point 90 located 52.5 mm from the corner and at 0.186 mm depth.

The time-integration scheme and time step are the same as for the preceding example. Fig. 4 displays snapshots of the particle velocity vector at $t = 0.06$ ms and $t = 0.09$ ms. In Fig. 4(a), the compressional wave has been diffracted by the corner while the Rayleigh wave is on the corner with the shear wave slightly in advance. A head wave connecting the body waves can also be observed. At 0.09 ms (Fig. 4(b)), the Rayleigh wave has been split into transmitted and reflected surface waves traveling vertically and horizontally, respectively. The event generated by the interaction of the shear wave with the vertical boundary can be clearly appreciated. This pulse travels with apparent infinite velocity at the corner and approaches c_S at infinite distance from the corner (see also Fig. 5). In Fig. 5, we show the response of the medium recorded at 0.186 mm from the surface. The first 60 receivers correspond to the upper boundary and the next 40 receivers to the right boundary of the step. The strong event is the Rayleigh wave which at 0.06 ms splits into transmitted and reflected Rayleigh waves.

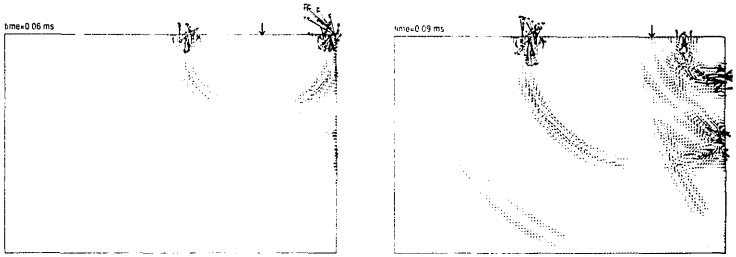

Fig. 4. Snapshots of the particle velocity vector for the step problem at 0.06 ms (a) and 0.09 ms (b). In (a), the Rayleigh wave produced by a vertical impact has reached the corner. The reflected and transmitted surface waves can be observed in (b).

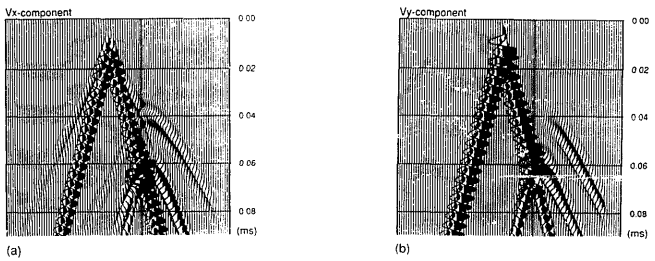

Fig. 5. Response of the step recorded at 0.186 mm from the surface, where (a) and (b) represent the v_x and v_y components, respectively. The first 60 receivers correspond to the upper boundary and the next 40 receivers to the right boundary of the step. The strong event is the Rayleigh wave which at 0.06 ms splits into transmitted and reflected Rayleigh waves.

4.3. Fine layering

This example illustrates the ability of the method to model a stack of fine layers, one of the most common geological structures appearing in sedimentary formations. It is well known that in the long-wavelength limit, the fine layering formation can be replaced by an equivalent transversely isotropic medium. A series of numerical experiments to illustrate this property in periodically layered media have been carried out by Carcione et al. [23], where they show that the replacement is valid for a dominant wavelength greater than nearly ten times the spatial period of the stratification. The grid geometry with $N_x = N_y = 81$ is shown in Fig. 6, where the fine concentration of points at the center of the mesh has been obtained by using the mapping function equation (15) with $\delta = 0$ and $\epsilon = 0.2$. In the horizontal direction, we apply the same mapping with $\delta = 0$ and $\epsilon = 0.4$. This shows that it is more effective to use mapping transformations to resolve the structure than to simply add more grid points into the physical coordinate system. The dimensions of the physical space are $x_{max} = 1000$ m and $y_{max} = 500$ m, with maximum and minimum grid spacing of $dx_{max} = 20$ m, $dy_{max} = 13$ m, and of $dx_{min} = dy_{min} = 0.96$ m, respectively.

The model structure and configuration is illustrated in Fig. 7. The structure is a periodic set of sandstone-limestone layers (from grid point 35 to grid point 47) of equal thickness embedded in homogeneous sandstone. The spatial period of the stratification is approximately 4 m, such that the total thickness of the system is 24.5 m. In [23] the values of the wave velocities and elastic constants of the equivalent medium can be found. At 40 m above the stack, a vertical force of 20 Hz dominant frequency excitates the medium. The response is recorded by a set of geophones located 40 m below the fine layering. The dominant wavelength to spatial period ratio for vertical incidence is 45 for the P waves and 25 for the S waves, so the long-wavelength approximation is satisfied.

The solution is propagated to 1.2 s with a time step of 0.25 ms by using a 4th-order Runge–Kutta integration scheme. Fig. 8 represents the seismograms for the fine layering system and equivalent transversely isotropic medium. As the pictures show, the match between solutions is virtually perfect. This example also constitutes a test of the performance of the differential operator in regions where sharp discontinuities of the material properties take place.

4.4. Lamb's problem by domain decomposition

This example consider two meshes (subdomains A and B) as displayed in Fig. 9. The vertical interface separating the subdomains can be a real material interface or just a boundary separating regions of the same medium. As before, the wave equation is decomposed into wave modes describing outgoing and

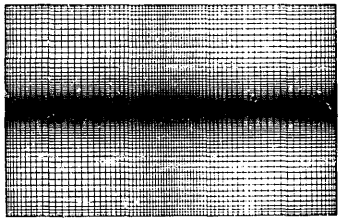

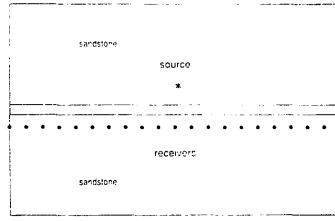

Fig. 6. Numerical mesh of the physical space for the fine layering problem. The mapping function (15) is used for both the horizontal and vertical directions. The region at the center of the mesh has vertical grid spacing of 2 m and represents a periodic sequence of sandstone-limestone layers.

Fig. 7. Structure and recording configuration of the fine layering problem. The sandstone-limestone sequence of 24.5 m total thickness is embedded in a homogeneous sandstone. The source is a vertical impact of 40 Hz dominant wavelength, so that the long-wavelength approximation is satisfied. The stack of layers is equivalent to a homogeneous transversely isotropic medium.

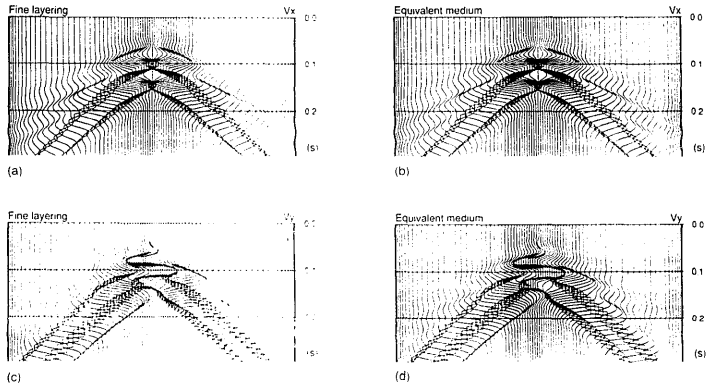

Fig. 8. Seismograms of the fine layered problem. (a) and (b) display the v_x-component, and (c) and (d) display the v_y-component. As can be observed, there is no difference between the solutions obtained from the stack of layers and the homogeneous anisotropic equivalent medium.

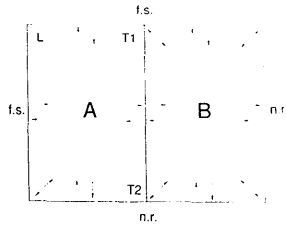

Fig. 9. Cartesian mesh composed of two Chebyshev subgrids (A and B). The directions of the characteristics are indicated in the Figure. The left and upper boundaries satisfy stress-free conditions, and the right and lower boundaries satisfy non-reflecting conditions.

incoming wave modes perpendicular to the boundary. The outgoing waves are determined by the solution inside the subdomain, while the incoming waves are calculated from the conditions at the interface, i.e. continuity of displacements and normal stresses. The boundary equations can be found in [2, 12].

Corners points, like L, for instance, are tested in the step example. Problems may arise from the so-called T points, which combine interface and free surface boundary conditions (T1), or interface and non-reflecting boundary conditions (T2). These points are treated independently (in each subdomain) with rotated characteristics. Unlike the interface points, where the wavefield is unique for both subdomains, T points have dissimilar values.

Here, we test the performance of the boundary treatment on T points, in particular, the intersection of the vertical interface with the free surface (point T1) (see Fig. 9). This type of singular points appears in many problems. For instance, consider a fluid-filled borehole. If the fluid and the Earth are given mesh A and B, respectively, the point fluid-solid-Earth surface is a T point.

We consider the medium homogeneous with compressional and shear velocities $c_P = 2000$ m/s and $c_S = 1300$ m/s, respectively, and a density of $\rho = 2$ g/cm^3. The source is a vertical force having a Ricker wavelet time-history with central frequency $f_0 = 16$ Hz. The force is in subdomain A at 1.87 m depth, and 372.8 m from the interface. Two receivers are located in subdomain B at 121 m from the interface, one at the surface and the other at 212.8 m depth. The calculations use a numerical mesh with $N_x = 81$ and $N_y = 121$ for each subdomain. Their dimensions after the stretching are $x_{\max} = 1460.3$ m and $y_{\max} = 2252.3$ m, with maximum grid sizes of $dx_{\max} = dy_{\max} = 20$ m at the centers of the meshes. The mapping function is given in Eq. (11) and the stretching parameters are $\alpha_x = 4.86$, $\alpha_y = 7.2$ and $\beta = 2$. We found from numerical tests that in order to maintain stability, the aspect ratio of the cells (maximum to minimum length) close to L and T points must be less than 5. The solution is propagated to 0.8 s with a time step of 1 ms.

Fig. 10 shows two snapshots of the particle velocity vector. Comparison between numerical and analytical time histories are represented in Fig. 11. As can be seen from the pictures, the results are satisfactory. The information is correctly transmitted from one subdomain to the other.

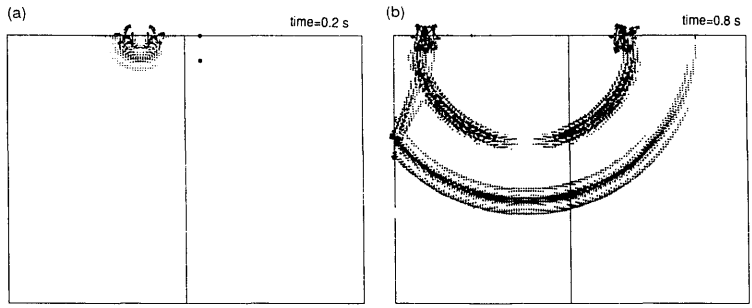

Fig. 10. Snapshots of the particle velocity vector at (a) 0.2 s and (b) 0.8 s. The source is in the left subdomain (A) and the receivers, represented by dots, are in the right subdomain (B).

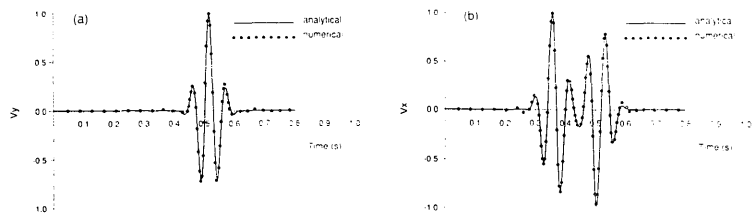

Fig. 11. Comparison between numerical and analytical solution at the two receivers located in domain B (indicated by dots in Fig. 10). (a) represents the v_y-component at the surface receiver, and (b) shows the v_x-component at the depth receiver.

5. Conclusions

We have solved the elastic wave equation with a 2D Chebyshev pseudospectral operator where general boundary conditions can be imposed, and the collocation points in the physical domain can be distributed in accordance with the structure of the model. This is achieved by mapping transformations which control the minimum grid spacing to render the algorithm efficient in terms of computational effort. Instabilities of the differential operator due to boundary conditions are solved with a characteristic approach. First, Lamb's problem tests the effectiveness of the 2D Chebyshev grid and boundary treatment by comparing numerical and analytical solutions. The performance of the corner points is tested by propagating a pulse through a surface step where the modeling reproduces correctly the transmitted and reflected Rayleigh waves. The third example shows how the grid can be adapted to a finely layered structure, and successfully tests the performance of the differential operator in the presence of sharp discontinuities in the material properties. Finally, the technique is used for domain decomposition where the subdomains can be joined by imposing the appropriate boundary conditions on the incoming waves at the interfaces. Lamb's problem is successfully solved for the source in one subdomain and the receivers in the other subdomain.

A natural extension of the method involves the use of 2D coordinate transformations such that the grid points can be adapted to topographic features and curved interfaces.

Acknowledgement

This work was funded in part by the European Commission in the framework of the JOULE programme, sub-programme Advanced Fuel Technologies.

References

[1] D. Kosloff, D. Kessler, A. Queiroz Filho, E. Tessmer, A. Behle and R. Strahilevitz, Solution of the equations of dynamic elasticity by a Chebychev spectral method, Geophys. 55 (1990) 734–748.
[2] E. Tessmer, D. Kessler, D. Kosloff and A. Behle, Multi-domain Chebyshev–Fourier method of the solution of the equation of motion of dynamic elasticity, J. Comput. Phys. 100 (1992) 355–363.
[3] D. Kessler and D. Kosloff, Acoustic wave propagation in 2D cylindrical coordinates, Geophys. J. Int. 103 (1990) 577–587.
[4] J.M. Carcione, Modeling anelastic singular surface waves in the Earth, Geophys. 57 (1992) 781–792.
[5] G.A. Raggio, Pseudo spectral Chebyshev scheme for forward acoustic modeling, Z. Angew. Math. Mech. 66 (1986) 545–553.
[6] D. Kosloff and H. Tal-Ezer, A modified Chebyshev pseudospectral method with an $O(N^{-1})$ time step restriction, J. Comput. Phys. 104 (1993) 457–469.
[7] J.M. Augenbaum, An adaptive pseudospectral method for discontinuous problems, Appl. Numer. Math. 5 (1989) 459–480.
[8] J.M. Augenbaum, Multi-domain adaptive pseudospectral methods for acoustic wave propagation in discontinuous media, in: D. Lee, A. Cakmak and R. Vichnevetsky, eds., Computational Acoustic, Seismo-Ocean Acoustics and Modeling (1990) 19–40.
[9] H. Lamb, On the Propagation of Tremors over the Surface of an Elastic Solid, Phil. Trans. R. Soc. London A203 (1904) 1–42.
[10] J.M. Carcione, Boundary conditions for wave propagation problems, Finite Elements Anal. Des. 16 (1994) 317–327.
[11] J.M. Carcione, Time-dependent boundary conditions for the 2D linear anisotropic-viscoelastic wave equation, Numer. Methods Part. Diff. Eqs. 10 (1994) 772–791.
[12] J.M. Carcione, Domain decomposition for wave propagation problems, J. Sci. Comput. 6 (1991) 453–472.
[13] Y.C. Fung, Foundations of Solid Mechanics (Prentice-Hall, Englewood Cliffs, NJ, 1965).
[14] D. Gottlieb and S. Orszag, Numerical analysis of spectral methods: Theory and applications, in: CBMS Regional Conference Series in Applied Mathematics 26 (SIAM, Philadelphia, PA, 1977).
[15] A. Solomonoff and E. Turkel, Global properties of pseudospectral methods, J. Comput. Phys. 81 (1989) 239–276.
[16] A. Bayliss, D. Gottlieb, B. Matkowsky and M. Minkoff, An adaptive pseudospectral method for reaction diffusion problems, J. Comput. Phys. 81 (1989) 421–443.
[17] D. Gottlieb, M. Gunzburger and E. Turkel, On numerical boundary treatment for hyperbolic systems, SIAM J. Numer. Anal. 13 (1982) 671–697.
[18] K.W. Thompson, Time-dependent boundary conditions for hyperbolic systems, II, J. Comput. Phys. 89 (1990) 439–461.
[19] I. Lie, Ocean/Bottom Acoustic Interaction with Arbitrary Bottom Profile, FFI/Rapport-91/7009, NDRE (1991).
[20] B.A. Auld, Acoustic fields and waves in solids, Volume 1 (Robert E. Krieger Publishing Co., Malabar, FL, 1991).
[21] R. Kosloff and D. Kosloff, Absorbing boundaries for wave propagation problems, J. Comput. Phys. 63 (1986) 363–376.
[22] J.F. Epperson, On the Runge example, Amer. Math. Monthly 94 (1987) 329–341.
[23] J.M. Carcione, D. Kosloff and A. Behle, Long-wave anisotropy in stratified media: A numerical test, Geophys. 56 (1991) 245–254.